International Journal of Autonomous Robotics and Intelligent Systems
Vol. 1, No. 2, December 2025 [129-142]

An Image Processing Approach for Quantitative Microstructural Analysis of Solid Oxide Fuel Cell Anodes

K. S. Tan[1*], C. K. Lam[1,2] and W. C. Tan[3]

[1]Faculty of Electrical Engineering & Technology, Universiti Malaysia Perlis, 02600 Arau, Perlis, Malaysia
[2]Centre of Excellence for Intelligent Robotics & Autonomous System (CIRAS), Universiti Malaysia Perlis, 02600, Arau, Perlis, Malaysia
[3]Faculty of Mechanical Engineering & Technology, Universiti Malaysia Perlis, 02600 Arau, Perlis, Malaysia

Received 24 October 2025, Revised 21 November 2025, Accepted 2 December 2025

ABSTRACT

Solid oxide fuel cells are emerging as promising devices for electrochemical energy conversion because they offer high efficiency and fuel flexibility. However, their performance is highly dependent on complex microstructural features that are difficult to quantify accurately. This research presents an image processing pipeline designed for segmenting and quantifying the microstructures of solid oxide fuel cells. The pipeline incorporates tailored techniques such as preprocessing, segmentation and morphological quantification analysis to handle the complexity of multiphase structures. Despite these efforts, segmentation accuracy remains a challenge due to issues like intensity overlap between different phases, surface or texture imperfections, and unclear boundaries. Consequently, the quantification accuracy ranged from 83.22 % to 99.49 %. Although some variation exists among the quantification parameters like particle size, volume fraction, and area interfacial density, the overall strong performance demonstrates the capability of automating solid oxide fuel cell image analysis. This work establishes a foundational framework for future improvements with the integration of machine learning or deep learning techniques to enable more accurate and reproducible characterization of solid oxide fuel cells.

Keywords: Image Segmentation, Image Quantification, Solid Oxide Fuel Cell, Microstructure

1. INTRODUCTION

Nowadays, hydrogen energy drives significant research interest in the global energy sector due to clean and sustainable energy sources. Among the technologies developed for hydrogen, solid oxide fuel cells (SOFC) stand out for their high efficiency, environmentally friendly and ability to operate with minimum emissions [1]. The working mechanism of SOFC eliminates the need for intermediate combustion steps. This is because SOFC directly transforms the chemical energy such as hydrogen or hydrocarbon gases into electrical and heat energy through electrochemical reactions [2]. A typical SOFC comprises a dense electrolyte sandwiched between two porous electrodes, namely the anode and cathode. Next, the fuel oxidation and oxygen reduction occur on the electrodes respectively [3]. Based on the developed electrolyte materials, yttria-stabilized zirconia (YSZ) is commonly selected due to its superior ionic conductivity [1][2]. Undeniably, each electrode is composed of mixed ionic and electronic conducting materials to form a complex multiphases microstructure and this type of multiphases microstructure plays an important role in governing the gas transport [3][4]. Nevertheless, the mass transport efficiency, electrochemical activity, and mechanical stability are easily impacted by porous electrodes [3].

During fabrication, SOFC operates at high temperatures between 600 °C to 1000 °C and requires even higher temperatures between 1200 °C and 1500 °C for the sintering process [5]. This

*karshen@studentmail.unimap.edu.my

extreme thermal environment can easily cause some complications, such as introducing unwanted chemical reactions, elemental interdiffusion among components and gradual deterioration of material properties [6]. Besides that, in the similar fabrication and operation process, structural deformation issues may arise if thermal expansion mismatches in electrodes under high temperature [5]. Although SOFCs are excellent in high energy efficiency and able to operate in various fuel types, their prolonged operation at high temperatures ranging from 600 °C to 900 °C can result in degradation. This issue is linked to microstructural changes within the electrodes and it will impact the long term performance and stability of fuel cells [7]. The microstructure of a SOFC includes several features, for example, boundaries, particle size and phase distribution. These features have a direct relationship to its electrochemical performance. Besides that, quantification of key parameters such as particle size, volume fraction, and interfacial area density is important because it helps to determine the performance of SOFC. There is also a list of microscopy imaging techniques utilized by researchers in investigating the microstructure, including scanning electron microscopy, electron backscattered diffraction, dual-beam focused ion beam with scanning electron microscopy (FIB-SEM) and transmission electron microscopy [8]. These techniques are widely used by material science researchers because the methods provide a direct spatial visualization on the microstructural features and reveal the internal structures and surfaces [9].

While microscopy imaging techniques like FIB-SEM are capable of producing high resolution two-dimensional (2D) images, the generation of large volume datasets remains a significant bottleneck. This challenge has been anticipated especially when addressing both specific requirements such as fine resolution and wide spatial coverage. Moreover, image acquisition speed and resolution are limited by the imaging hardware and this causes high throughput analysis of porous structures difficult to analyze [9]. The porous architecture of SOFC electrodes poses additional challenges during data acquisition and processing as well. For instance, imaging artifacts such as curtaining, charging effects and poor defined phase boundaries are common, and the back-pore phenomenon can further obscure surface features from the pores itself [10][11]. Thus, reliably extracting useful information from these complex datasets remains a major hurdle [8]. In most cases, the segmentation of ground truth microstructural images is still performed manually. Since the ground truth images are arranged sequentially, scientists or trained experts visually inspect and annotate each image by referring to the preceding and following images in order to distinguish between phases. Although this method yields accurate interpretation, it is labour intensive and prone to inconsistency especially when multiple scientists are involved [8][12]. Variability in judgments or decision calls can lead to inconsistencies across large datasets and limit the reproducibility [13].

After segmenting microstructural images, image quantification is a critical step that translates the visual features into meaningful metrics. The quantification parameters such as particle size, volume fraction and interfacial area density are extracted to determine the relationship between the microstructural characteristics and electrochemical behavior of the cell's performance. However, the accuracy of these metrics depends heavily on the quality of the initial segmentation and the computational algorithms applied. Poor segmentation introduces errors that propagate through the analysis and produce inconsistent results. Consequently, the data quality issues and uncertainty become more complicated in subsequent analyses [14]. Given these challenges, there is a growing interest in developing automated and intelligent image processing techniques to enhance the precision and reproducibility of microstructural quantification.

1.1 Image Processing Framework

Image processing forms the backbone of automated microstructural analysis and allows researchers to extract useful information from images more efficiently. This technique has applied beyond material sciences from satellite imaging and medical diagnostics to robotics and remote sensing [15]. On the other hand, image processing involves the computational

manipulation and analysis of visual data in 2D images to improve the image clarity or extract information from the image [16]. This approach mirrors how our own visual system works, where the eyes capture a scene but it is the brain's interpretation that determines what we actually see [16].

Furthermore, image processing generally falls into two main categories: analog and digital. While analog processing deals with manipulating physical signals or media, digital image processing uses computer algorithms to analyze and improve digital images [17]. Digital image processing has become dominant due to its flexibility and scalability [17]. The image processing process starts with capturing images using devices like microscopes, cameras, or satellites [17]. Since ground truth images frequently contain noise or incompleteness, preprocessing is an essential step to clean the data before analysis. As Maharana et al. [18] highlighted, poor quality images can lead to inaccurate results. Hence, preprocessing techniques like noise reduction, filtering, and unwanted distortions removal are applied to enhance image clarity [18][19]. Besides that, image enhancement methods such as histogram equalization and contrast enhancement are used to reveal hidden details and support more reliable downstream analysis [17]. Feature extraction plays a central role in image classification as it transforms raw pixel data into descriptive numerical features that highlights the important aspects of the image, such as edges, textures and contours [19]. These features are normally categorized as local or global depending on whether they describe specific regions or image characteristics like shape, color and texture [20]. The effectiveness of a classification model depends on how well the features represent the underlying structure in the image. Feature extraction sets the stage for image segmentation and image segmentation itself is a key step in image processing and computer vision. By dividing an image into unique and non-overlapping regions, segmentation makes it easier to isolate specific objects or features [21]. Additionally, this simplifies the image for interpretation but also reduces the computational effort by limiting subsequent analysis to smaller regions of interest [22][23].

Once the SOFC microstructure has been segmented into distinct regions, the next step involves quantifying microstructural properties. One of the most critical parameters is particle size which influences gas diffusion within the electrode for faster transportation of electrons and ions, respectively [24]. For example, Nenning et al. [25] observed that the average particle size should ideally be much smaller than the electrode thickness to maintain continuous and effective conduction pathways, so that the electrode can be modelled as a homogeneous medium. In addition, another important parameter is volume fraction which describes the proportion of each phase within the microstructure. This value affects the amount of active material available for electrochemical activity and thus influences the fuel cell power. In a mesoscale study, Mahbub et al. [26] examined the Ni and pore phases distributions in identical YSZ anodes and found that local variations in particle size and volume fraction altered electrode performance. Similarly, Sun et al. [27] reported that increasing the volume fraction of the ion-conducting phases not only improved initial performance but also mitigated long term degradation. This is because the higher the proportion of the phase, the faster the uniform distribution of reaction rates [27]. Notably, the particle size and volume fraction are interdependent. Smaller particle sizes reach the percolation threshold when the volume fractions are lower [28]. So, particle size and volume fraction composition of each phase must be always considered [29].

Meanwhile, the interfacial area density reflects how extensively phases such as Ni and YSZ are connected in microstructure. This parameter focuses on determining the number of active electrochemical sites. According to Xiang et al. [29], the changes in Ni and pore volume fractions affect anode stability by influencing degradation processes at the nickel-yttria-stabilized zirconia (Ni-YSZ) interface. In addition, by increasing the interfacial area of Ni-YSZ, the anode stability also increases and this happens even when the Ni particles are relatively small [29]. Furthermore, larger interfacial area also helps to reduce the system overall energy [30]. In conclusion, classical image processing methods, such as filtering, enhancement, and thresholding are applied for automated segmentation of SOFC microstructural images. These interpretable and controllable

techniques enable consistent quantification of microstructural properties like particle size, volume fraction, and Ni-YSZ interfacial area density, clarifying their influence on electrochemical performance.

2. METHODOLOGY

The methodology outlined in Figure 1 uses a systematic approach to analyze and quantify SOFC anode images through image processing techniques. It follows a structured workflow that includes multiple stages, for example, image acquisition, preprocessing, segmentation and quantitative analysis to identify and measure microstructural features. The process starts with preparing a curated set of SOFC images that represent a variety of structural conditions. These images are then proceeded to preprocessing steps such as filtering and enhancement to reduce noise and standardize the image quality. In order to further improve the image clarity, contrast adjustment is applied to improve visibility of different phases and structural details. After that, image segmentation is utilized to isolate specific features within the microstructure. Based on the segmented images, quantitative metrics like particle size, volume fraction, and interfacial area density are calculated. These measurements are crucial for understanding the material characteristics and SOFC anode fuel cell performance. Finally, the computed results obtained from the automated segmentation are compared with reference data. This comparison helps to evaluate the accuracy of image processing algorithms used for image segmentation and image quantification.

This research utilized a dataset provided by a research group at Kyoto University. The dataset comprises 80 SOFC images, each with dimensions of 305 by 285 pixels (height by width) as presented Figure 2. The dataset was selected because its quantification results were previously published in Kishimoto et al. [31] and this served as a reliable reference for validation. By referencing these results, the accuracy of the image quantification process can be effectively evaluated.

Firstly, the ground truth image is converted from red, green, and blue format to grayscale. This simplifies the image by reducing it to a single intensity channel and eliminates unnecessary complexity that can arise from multiple colour formats. After that, a Gaussian filter which is known as a linear smoothing filter [32] is applied to improve the visibility of fine microstructural details. In Tan et al. [33], a Gaussian filter with a radius of two pixels was used to reduce image noise. The higher the kernel radius, the smoother the image becomes. However, this will cause excessive smoothing and loss of important microstructural details. Therefore, it is important to balance the noise reduction and details preservation. Moreover, the smoothed image is subjected to brightness enhancement and median filtering, a non-linear filtering technique [34] to simultaneously amplify high frequency components like edges, structural transitions, and phase boundaries while also preserving the intricate image details [34]. In addition, Rix et al. [35] mentioned that median filter is particularly effective in eliminating single pixel and two pixel misclassifications. This combination not only clarifies darker regions but also acts as a brightness normalization step where the intensity values are linearly rescaled. The image is normalized again by scaling pixel values from the original range of 0 to 255 to a standardized range of 0 to 1. Subsequently, multi-level thresholding is applied to divide the image into distinct regions by identifying multiple optimal thresholds. As described in Equation (1), these thresholds are selected to maximize the inter-class variance in order to separate the boundaries between different structural phases [36]:

$$[t_1, t_2, t_3, \dots, t_{K-1}] = \text{ArgMax}\sigma^2_{between-class}(t) \quad (1)$$

where, t = threshold value and K = class.

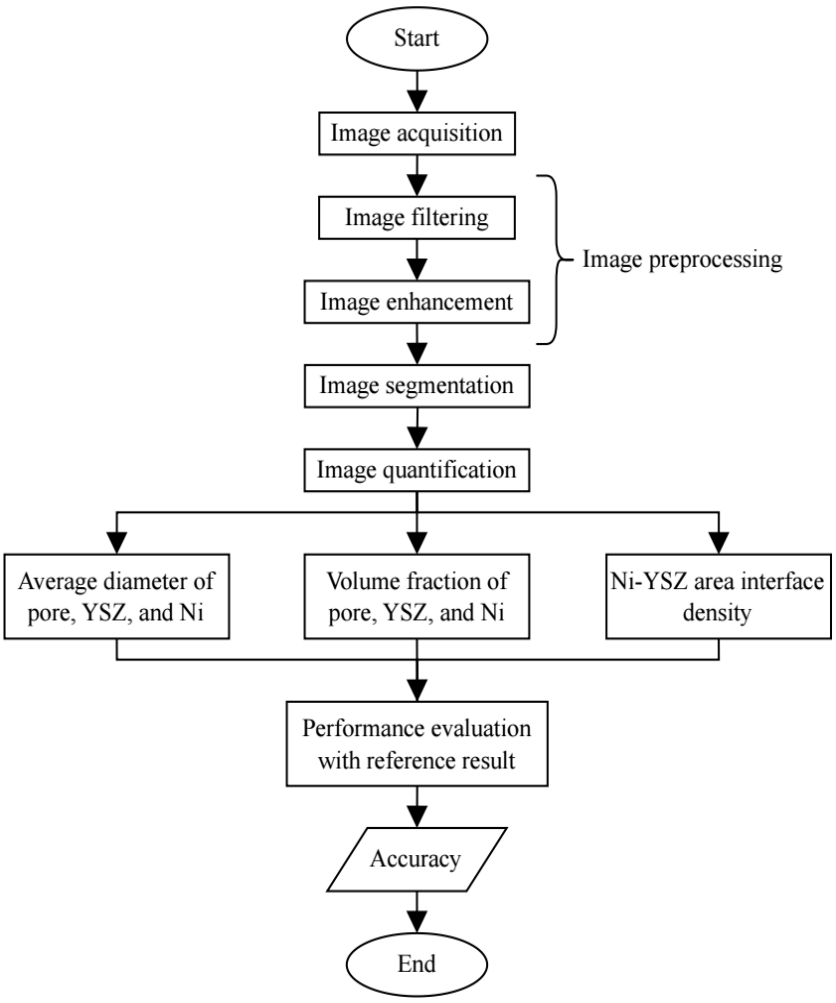

Figure 1. Flowchart of SOFC image processing workflow

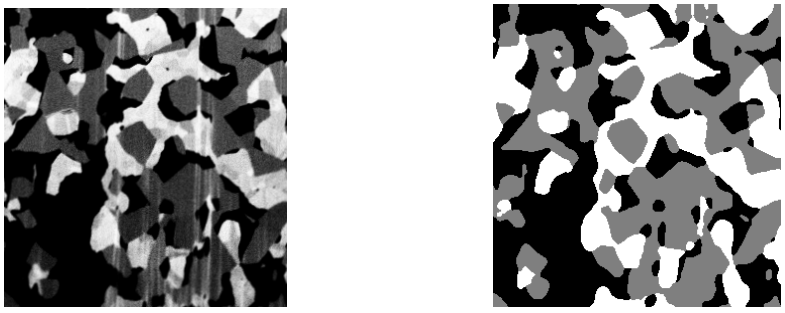

Figure 2. SOFC images: (a) Ground truth SOFC image, and (b) manual segmented image [31]

In Chen and Gao [37] research on the fuel cell, a multi-level thresholding image segmentation technique was used to segment the gas diffusion layer for an accurate separation of pores, fibres and binder phases. Since the SOFC image exhibits three distinct intensity levels, corresponding to black, gray, and white regions which represent the pore, YSZ, and Ni phases respectively as presented in Figure 3, multi-level thresholding is an appropriate segmentation approach. This method suits multiphase images as it determines more than one optimal threshold value to partition the image into separate regions based on intensity distributions. After multi-level thresholding, three distinct masks corresponding to the three main phases are produced.

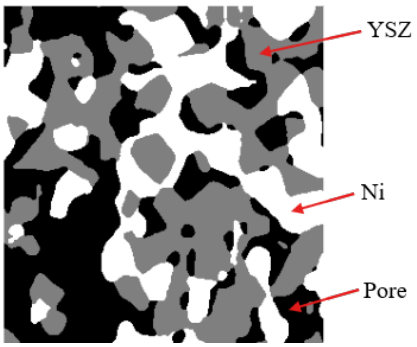

Figure 3. Labelled SOFC components on manual segmented SOFC image

Next, three quantitative analyses are carried out to characterize the SOFC microstructure: particle size of pore, YSZ, and Ni; volume fraction of pore, YSZ, and Ni, and Ni-YSZ interfacial area density. The line intercept method is utilized on each mask to quantify the average phase diameter, drawing on the methodologies proposed by Sciazko et al. [38] and Yamazaki et al. [39]. In Sciazko et al. [38], a grid of lines is superimposed along orthogonal directions and the intercepts formed with each phase are measured to obtain the mean intercept length and its corresponding statistical distribution [38]. Yamazaki et al. [39] demonstrated a similar approach [40], as depicted in Figure 4 to quantify the phase connectivity. In their study, pore size is measured by using the distance between each pore voxel and its nearest solid voxel and multiplying by the voxel dimension [39]. By combining the principles of previous studies, the line intercept method provides a comprehensive framework for quantifying SOFC microstructural features.

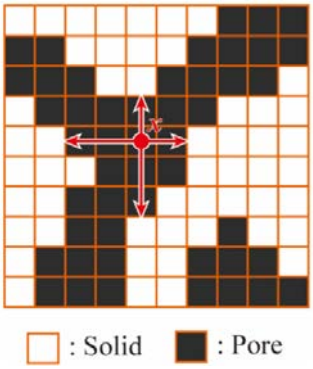

Figure 4. Schematic diagram of line intercept method [39]

For volume fraction, each phase is calculated to describe its spatial proportion within the structure. In Zhang et al. [41], voxel connectivity is established based on three-dimensional (3D) domain and nineteen-velocity lattice Boltzmann configuration where each voxel interacts with eighteen neighbouring voxels across adjacent faces and edges, excluding the eight corner voxels [41]. According to Zhang et al. [41] and Masashi Kishimoto [42], the volume fraction in 3D represents the ratio between the number of voxels belonging to a particular phase and the total number of voxels in the analyzed volume as shown in Equation (2):

$$V_l = \frac{Vol_l}{Vol_{all}} \tag{2}$$

where, V_l = the volume fraction of phase l and Vol = the volume [42].

When applied to the distinct masks, the same principle is adopted but expressed in terms of pixels rather than voxels. Consequently, the volume fraction of each phase is calculated by dividing the number of pixels representing that phase by the total number of pixels in the similar mask.

Hamann et al. [43] compared 2D and 3D analyses of Li-ion conducting electrolytes by looking at 2D area fraction and their corresponding 3D volume fractions. They found out that the 2D measurements provided a reliable approximation of the true 3D values as long as there is an extra margin of $\pm 1\%$ is added to the standard deviation of the 2D area fractions [43]. On the other hand, the surface area of each individual phase within the SOFC microstructure can be quantitatively estimated from the image using stereological relations as expressed in Equation (3):

$$S_v = 2P_L = \frac{4}{\pi} L_A \tag{3}$$

where, S_v = surface of phase in the volume, P_L = number of intersection points with curves or lines per unit length of probe line, L_A = total length of perimeter of phase per unit area [44].

Based on the individual surface area values, the interfacial area density between any two phases can be subsequently determined. For the Ni-YSZ interfacial area density calculation, the SOFC image after multi-level thresholding has been segmented into three distinct binary masks representing the pore, YSZ, and Ni phases. For the evaluation of interfacial properties, the boundaries of each phase need to be extracted. This is done by calculating the perimeter of each binary mask that highlights the pixel edges of each phase. There is a relationship between the interfacial area density and the overlapping regions between different phases. Since the total surface area of a phase can be represented as the sum of its interfaces with the other two phases, the interfacial area density between Ni and YSZ can be derived using Equation (4) [45]:

$$S_{Ni,YSZ} = \frac{S_{Ni} + S_{YSZ} + S_{pore}}{2} \tag{4}$$

Zhang et al. [46] noted that FIB-SEM and X-ray computed tomography are commonly used to reconstruct 3D microstructure of porous materials for accurate measurement of geometric properties. The properties included internal surface area, connectivity and porosity. While these imaging techniques avoided the need for empirical assumptions, but they are costly, time consuming, and not widely accessible in many laboratories [46]. They also pointed out that the interfacial area calculated from 2D analyses can closely match with the results obtained from 3D reconstructions. By using a 2D stereological approach, the measured Ni-YSZ interfacial area was 0.3357 ± 0.3612 $\mu m^2/\mu m^3$ which aligned closely with the 3D value of 0.3353 $\mu m^2/\mu m^3$ [46]. After completing the overall quantification of all microstructural parameters, their respective results are assessed by comparing with those from Kishimoto et al. [31] to verify the consistency and reliability of the automated image processing methods.

3. RESULTS AND DISCUSSION

This section presents the automated image processing and quantification techniques applied to analyze the SOFC microstructure. The proposed pipeline integrates several important steps: image preprocessing, phase identification and quantitative analysis of microstructural parameters. The performance of this pipeline is demonstrated through experimental results and followed by a discussion of its accuracy and consistency when compared to the reference study.

3.1 Image Analysis Results

Figure 5 provides a detailed illustration of the preprocessing steps applied to the SOFC microstructural images. In Figure 5(a), the original microstructure that contains variations in illumination, texture scratches and noise is shown as ground truth image. These variations can complicate the accuracy of phase segmentation easily. In order to mitigate these challenges, the image is first converted to grayscale as shown in Figure 5(b). This step is useful in removing color information. Continuously, as presented in Figure 5(c), a Gaussian filter is applied to suppress the noise level and smooth out the local intensity variations and surface imperfections while

maintaining the core morphological features of the microstructure. In practice, it functions as a combination of background estimation and background correction. By employing a large 81×81 kernel size which is equivalent to forty pixels of kernel radius, it captures the low frequency background details and approximates the uneven illumination observed in SOFC images. This is because the uneven illumination is potentially caused by uneven microscope's illumination [47]. After that, the estimated background is subtracted to enhance the microstructural edges. The selection of kernel size is guided by Yuan et al. [48] who noted that the maximum useable kernel size depends on image dimensions and frequency spectrum of the blur kernel. A large motion blur kernel may lose high frequency detail like ringing artifacts [48], but this is acceptable because the focus is on background estimation and not the full image recovery.

Lastly, Figure 5(d) shows the result after brightness enhancement with a value of 1.2 and median filtered. The brightness enhancement value selected indicates that the image brightness is increased proportionally by a factor of 1.2 and the image brightness will be 20 % higher than the original image. According to the brightness range comparison by Kandel et al. [49], the most effective enhancement range is determined as 0.5 to 1.25. This range helps to maintain the brightness adjustments close to original brightness level to yield the best performance [49]. For median filtering, 7×7 kernel size is a commonly used kernel sizes [50] and therefore is selected to apply strong smoothing in order to remove the texture scratches and noise. Dehghananari and Hosseinjanizadeh [51] reported that median filter produces a smoother image and effectively reduces noise when a large 7×7 kernel size is used. Nevertheless, the value chosen for the brightness enhancement and the selected median filter kernel size are important because they directly affect the amount of brightness increases and the amount of texture scratches and noise reduction. These steps can influence the phase boundary details loss if the values are too excessive. All parameter values were optimized through an iterative process that involved preliminary trials and visual inspections. A trade-off between noise suppression and preservation of microstructural details is carefully addressed in order to achieve the best image contrast and clarity.

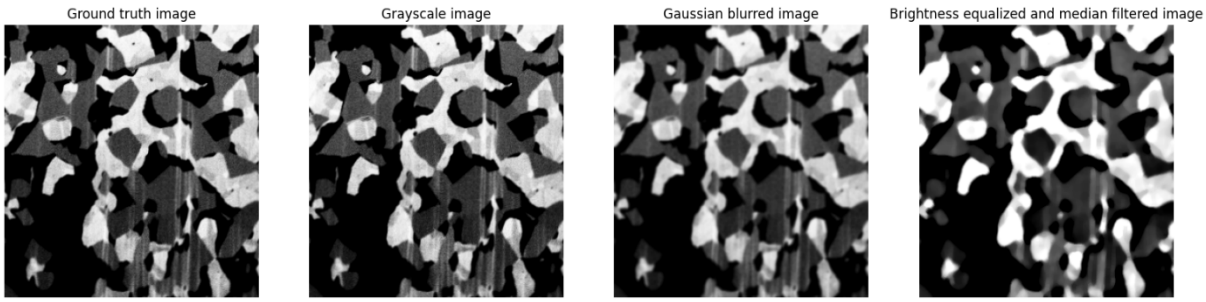

Figure 5. SOFC image after conducting image preprocessing: (a) Ground truth image, (b) grayscale image, (c) Gaussian blurred image, and (d) brightness equalized and median filtered image

Besides that, Figure 6 shows a comparison of different segmentation results after the SOFC image preprocessing. In Figure 6(a), the brightness equalized and median filtered image is used as a reference to assess the accuracy of the segmentation result of all phases. Figure 6(b) highlights an example of undersegmentation. As illustrated in the red circle, the pore particle size appears smaller when comparing it to Figure 6(a). This indicates a loss of structural pore details. In addition, Figure 6(c) demonstrates oversegmentation results. The blue circle marks irrelevant regions that are incorrectly identified. The misclassification happened along the boundary between the pore and Ni phases as represented in black and white in Figure 6(a). This will indirectly affect the computed results of particle size and volume fraction of pore and YSZ because the interfacial boundaries are interpreted as YSZ phase. In Figure 6(d), some Ni phases are incorrectly marked. These errors presented in the green circled area are potentially caused by

surface scratches that appeared during the preparation of ground truth image. Based on the discussed results, this shows that the proposed image processing methods are sensitive to surface artifacts.

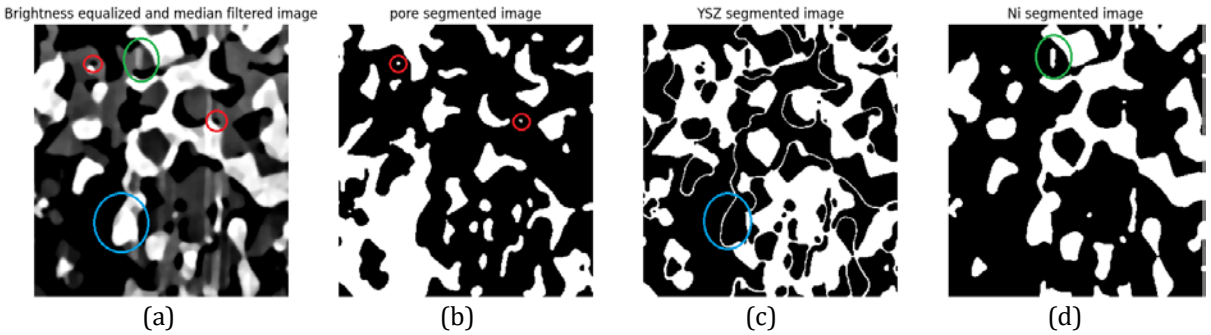

Figure 6. Comparison between phases in SOFC image after conducting image preprocessing: (a) Brightness equalized and median filtered image, (b) pore segmented image, (c) YSZ segmented image, and (d) Ni segmented image

In Shimura et al. [52] image processing workflow, the edge lines of the trimmed FIB-SEM grayscale images are first skeletonized to remove boundaries noise. The grayscale values are adjusted to ensure skeletonized edges formed closed regions. For each region, the mean grayscale value is used to identify its phase and assign the appropriate corresponding grayscale value [52]. If there were any segmentation errors, those are addressed manually and the skeleton lines are removed by replacing them with grayscale value of adjacent pixels [52]. After that, a 3D median filter is applied to smooth the image. In contrast, the tailored image processing approach used in this study is simpler and more efficient. Skeletonization is not required by avoiding the additional steps and computational cost associated with Shimura et al. [52] pipeline. 2D median filter is utilized in this research rather than a more complex 3D median filter. In Faes et al. [53], they used grayscale thresholding and morphological operations such as dilation and erosion with an octagonal structuring element to refine boundaries. The tailored pipeline presented here retained clear phase boundaries of SOFC without the need for these extra procedures.

Image quantification is performed using a dataset of 80 images provided by Kyoto University 's research team and the final results for each key metric representing the average measurements across the entire dataset. Table 1 summarizes the quantitative comparison between the reference results from Kyoto University's research team and the results obtained through automated image quantification. The analysis focuses on three key metrics: particle size, volume fraction, and Ni-YSZ interfacial area density for all phases. For the particle size, the reference results show 0.961 µm for pore, 1.210 µm for YSZ and 1.470 µm for Ni. In comparison, the automated quantification reported smaller values, 0.900 µm, 1.050 µm and 1.400 µm for the same respective phases. Their corresponding accuracies are 93.65 %, 86.78 % and 95.24 %. These discrepancies are likely due to factors previously mentioned such as the segmentation errors at phase boundaries, noise, and surface or texture scratches. These texture imperfections and image artifacts affected the segmentation algorithm to differentiate the tiny morphological details that are important in distinguishing between phases. So, the segmentation algorithm struggled to classify the regions correctly, especially in YSZ.

The volume fraction results show notable consistency. The Ni phase demonstrated highest accuracy at 99.49 %, while the pore and YSZ phases also presented high accuracies between 95.88 % and 97.83 %, showing clear intensity distinctions among phases. As shown in Figure 6(a), certain regions between pore and YSZ are difficult to differentiate because their grayscale intensities are too close yet the proposed algorithm effectively resolved these overlaps with precise segmentation. The Ni-YSZ interfacial area density yielded the lowest accuracy at just

83.22 % compared with other key parameters. This shows some missed or incorrectly detected interfaces. As depicted in Figure 7, the misclassification often occurs when pores are confused with YSZ due to low boundary contrast or when surface scratches within the YSZ are wrongly identified as Ni. As a result, these issues will significantly affect the segmentation accuracy and indirectly affect the quantification accuracy. Nevertheless, the automated approach attains high accuracy with results comparable to manual segmentation. Although there is a slight accuracy difference remaining, this automated approach offers a significant advantage in terms of efficiency and eliminates the need for labour intensive and time consuming manual annotation processes. In order to address the challenges introduced by image artifacts, machine learning or deep learning provide a promising platform. By learning directly from the ground truth images, the machine learning models can capture the phase patterns and texture representations needed to minimize the misclassification error. They are also capable of denoising the input images without any explicit filtering while preserving fine-scale features that traditional segmentation methods tend to overlook [54]. As demonstrated in Otic and Kinefuchi [55], a machine learning 3D reconstruction framework was able to effectively mitigate the slice-wise segmentation artifacts, image noise, and imaging resolution trade-off in FIB-SEM images.

Table 1 Quantification results comparison between Kyoto University's research team and automated image quantification

Phase	**Results by Kyoto University's Research Team**			**Results by using Automated Image Quantification**		
	Particle size (μm)	Volume fraction	Ni-YSZ interfacial area density ($\mu m^2/\mu m^3$)	Particle size (μm)	Volume fraction	Ni-YSZ interfacial area density ($\mu m^2/\mu m^3$)
pore	0.961	0.243	0.745	0.900	0.233	0.870
YSZ	1.210	0.368		1.050	0.376	
Ni	1.470	0.389		1.400	0.391	

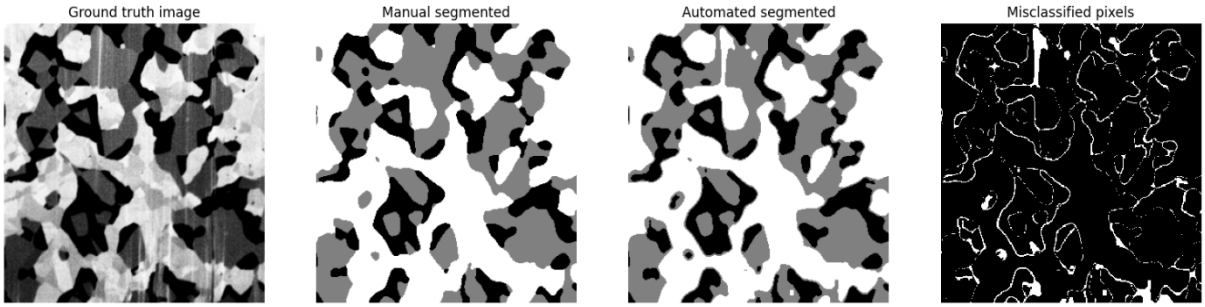

Figure 7. Comparison of segmented results: (a) Ground truth image, (b) manual segmented image, (c) automated segmented image, and (d) misclassified pixels

4. CONCLUSION

This study developed a tailored image processing pipeline for segmenting and quantifying the microstructural images of SOFC anode and evaluated its performance against manual segmentation. The tailored pipeline offers a distinct advantage over standard image processing workflows for SOFC microstructures. Conventional workflows rely on skeletonization and multiple morphological operations to suppress the phase boundaries noise and the proposed approach delivers precise phase boundaries without these additional steps. Several key microstructural parameters: particle size, volume fraction and the interfacial area density

between Ni and YSZ phases are calculated to assess accuracy. The automated approach showed minor oversegmented and undersegmentation, indicating a need for further refinement and optimization of the segmentation process. The quantified parameters achieved accuracies ranging from 83.22 % to 99.49 %, reflecting strong performance across most measurements despite some inconsistencies linked in segmentation errors. Image artifacts and overlapping intensities between phases were major error sources, challenging precise segmentation. Nonetheless, the imaging pipeline demonstrated its functionality and laid a solid foundation for future improvements. Given the complexity of SOFC images, conventional methods reached their limits, highlighting the potential of machine learning or deep learning approaches to capture complex patterns and enhance segmentation and quantification accuracy.

ACKNOWLEDGEMENTS

The authors gratefully acknowledge Prof. Hiroshi Iwai from Kyoto University for sharing the ground truth and segmented FIB-SEM data of the solid oxide fuel cell anode.

REFERENCES

[1] Y. Xu, D. Cui, H. Zhao, T. Li, R. Xiao, 2024. Prediction of electrode microstructure of SOFC with conditional generative adversarial network, International Journal of Hydrogen Energy, vol. 96, pp. 419-426, doi: 10.1016/j.ijhydene.2024.11.158.

[2] K. Steier, V. Guski, S. Schmauder, 2021. Numerical investigations on the damage behaviour of a reconstructed anode for solid oxide fuel cell application, Energies, vol. 14, no. 23, pp. 8082, doi: 10.3390/en14238082.

[3] X. Zhang, D. Yang, M. Xu, A. Naden, M. Espinoza-Andaluz, T. Li, John. TS. Irvine, M. Andersson, 2023. Analysing tortuosity for solid oxide fuel cell anode material: Experiments and modeling, Journal of The Electrochemical Society, vol. 170, no. 9, pp. 094502, doi: 10.1149/1945-7111/acf884.

[4] W. F. Kent, W. K. Epting, H. W. Abernathy, P. A. Salvador, 2025. Automated phase segmentation with quantifiable sensitivities of three-phase microstructures of solid oxide cell electrodes, Materials Characterization, pp. 115201, doi: 10.1016/j.matchar.2025.115201.

[5] W. Li, S. Wu, J. Zhu, W. Guan, E. Jin, H. Liu, 2025. Digital image correlation technique for full-field deformation of SOFC at 1300 ℃: An efficient speckle pattern for porous and diffusible substrates, Optics and Lasers in Engineering, vol. 186, pp. 108849, doi: 10.1016/j.optlaseng.2025.108849.

[6] Y. Zhang, L. Shen, Y. Wang, Z. Du, B. Zhang, F. Ciucci, H. Zhao, 2022. Enhanced oxygen reduction kinetics of IT-SOFC cathode with $PrBaCo_2O_{5+\delta}/Gd_{0.1}Ce_{1.9}O_{2-\delta}$ coherent interface, Journal of Materials Chemistry A, vol. 10, no. 7, pp. 3495-3505, doi: 10.1039/D1TA09615J.

[7] A. Sciazko, Y. Komatsu, T. Shimura, N. Shikazono, 2024. Prediction of electrode microstructure evolutions with physically constrained unsupervised image-to-image translation networks, npj Computational Materials, vol. 10, no. 1, pp. 49, doi: 10.1038/s41524-024-01228-3.

[8] GX. Zhang, Y. Song, W. Zhao, H. An, J. Wang, 2022. Machine learning-facilitated multiscale imaging for energy materials, Cell Reports Physical Science, vol. 3, no. 9, pp. 101008, doi: 10.1016/j.xrcp.2022.101008.

[9] Z. Niu, Z. Zhou, P. Perrenot, C. Villevieille, W. Zhao, Q. Cai, V. J. Pinfield, Y. Wang, 2025. Seeing the Middle: Reconstructing 3D Internal Electrode Microstructures from Low-Resolution Surfaces from Generative Diffusion Artificial Intelligence, Small Science, pp. e202500414, doi: 10.1002/smsc.202500414.

[10] B. Winiarski, P. Barthelemy, C. Jiao, D. Laeveren, D. Cox, S. A. Barnett, 2024. Solid Oxide Cells: from 3D Microstructure to Comprehensive Quantification, Microscopy and Microanalysis, vol. 30, pp. 305-306, doi: 10.1093/mam/ozae/044.139.
[11] H. Hwang, J. Ahn, H. Lee, J. Oh, J. Kim, J. P. Ahn, H. K. Kim, J. H. Lee, Y. Yoon, J. H. Hwang, 2021. Deep learning-assisted microstructural analysis of Ni/YSZ anode composites for solid oxide fuel cells, Materials Characterization, vol. 172, pp. 110906, doi: 10.1016/j.matchar.2021.110906.
[12] A. Nanjundappa, 2022. Morphological Characterization of Microporous Layers for Polymer Electrolyte Fuel Cells, [Master's thesis, School of Mechatronic Systems Engineering, Simon Fraser University]. Simon Fraser University Summit Research Repository. https://summit.sfu.ca/item/35274.
[13] M. Chalusiak, W. Nawrot, S. Buchaniec, G. Brus, 2021. Swarm intelligence-based methodology for scanning electron microscope image segmentation of solid oxide fuel cell anode, Energies, vol. 14, no. 11, pp. 3035, doi:10.3390/en14113055.
[14] EO. Brenne, 2021. Statistical Methods for Quantification and Segmentation of Material Microstructure from 3D X-ray Tomography Image Data, [Doctoral dissertation, Department of Energy Conversion and Storage, Technical University of Denmark]. DTU Research Database. https://orbit.dtu.dk/en/publications/statistical-methods-for-quantification-and-segmentation-of-materi
[15] S. Boopathi, U. K. Kanike, 2023. Applications of artificial intelligent and machine learning techniques in image processing, Handbook of Research on Thrust Technologies' Effect on Image Processing, igi global, pp. 151-173, doi: 10.4018/978-1-6684-8618-4.ch010.
[16] N. R. S. Muda, B. Faranadila, M. F. Fadilah, 2024. Implementation of Multisensor to Detect Vibration, Sound and Image of Combat Vehicles Use Artificial Neural Networks, International Journal of Innovative Science and Research Technology, vol. 9, no. 2, pp. 1217-1223, doi: 10.5281/zenodo.10720432.
[17] H. Ali, 2024. A Comprehensive Overview of Digital Image Processing: Techniques, Application, and Evolving Technologies, ILMA Journal of Technology & Software Management (IJTSM), vol. 5, no. 1, pp. 1-15.
[18] K. Maharana, S. Mondal, B. Nemade, 2022. A review: Data pre-processing and data augmentation techniques, Global Transitions Proceedings, vol. 3, no. 1, pp. 91-99, doi: 10.1016/j.gltp.2022.04.020.
[19] B. Sistaninejhad, H. Rasi, P. Nayeri, 2023. A review paper about deep learning for medical image analysis, Computational and Mathematical Methods in Medicine, vol. 2023, no. 1, pp. 7091301, doi: 10.1155/2023/7091301.
[20] M. Bansal, M. Kumar, M. Sachdeva, A. Mittal, 2023. Transfer learning for image classification using VGG19: Caltech-101 image data set, Journal of Ambient Intelligence and Humanized Computing, vol. 14, no. 4, pp. 3609-3620, doi: 10.1007/s12652-021-03488-z.
[21] L. Antonelli, V. De. Simone, D. di. Serafino, 2022. A view of computational models for image segmentation, ANNALI DELL'UNIVERSITA'DI FERRARA, vol. 68, no. 2, pp. 277-294, doi: 10.1007/s11565-022-00417-6.
[22] M. E. Rayed, S. S. Islam, S. I. Niha, J. R. Jim, M. M. Kabir, M. F. Mridha, 2024. Deep learning for medical image segmentation: State-of-the-art advancements and challenges, Informatics in medicine unlocked, vol. 47, pp. 101504, doi: 10.1016/j.imu.2024.101504.
[23] A. M. Ashir, 2022. Multilevel thresholding for image segmentation using mean gradient, Journal of Electrical and Computer Engineering, vol. 2022, no. 1, pp. 1254852, doi: 10.1155/2022/1254852.
[24] P. Blaszczak, A. Ducka, B. Wolanin, K. Matlak, G. Machowski, M. Prześniak-Welenc, S. F. Wang, B. Bochentyn, P. Jasiński, 2023. Fabrication of wormhole-like YSZ and Ni-YSZ by the novel soft-hard template CTAB/NACl-assisted route. Suppressing Ni coalescence in SOFC, Journal of European Ceramic Society, vol. 43, no. 2, pp. 438-451, doi: 10.1016/j.jeurceramsoc.2022.09.054.

[25] A. Nenning, C. Bischof, J. Fleig, M. Bram, A. K. Opitz, 2020. The relation of microstructure, materials properties and impedance of SOFC electrodes: a case study of Ni/GDC anodes, Energies, vol. 13, no. 4, pp. 987, doi: 10.3390/en13040987.
[26] R. Mahbub, T. Hsu, W. K. Epting, G. Nolan, Y. Lei, N. T. Nuhfer, R. B. Doane, H. W. Abernathy, G. A. Hackett, S. Litster, A. D. Rollett, 2021. Quantifying morphological variability and operating evolution in SOFC anode microstructures, Journal of Power Sources, vol. 498, pp. 229846, doi: 10.1016/j.jpowsour.2021.229846.
[27] M. Sun, A. Li, Y. Fei, Z. Chen, L. Zhu, Z. Huang, 2025. Microstructural Evolution-Driven Degradation of Nickel-Based SOFC Anodes: Insights from Mesoscale Modeling, Electrochimica Acta, vol. 541, pp. 147454, doi: 10.1016/j.electacta.2025.147454.
[28] B. Timurkutluk, Y. Ciflik, T. Altan, O. Genc, 2022. Synthetical designing of solid oxide fuel cell electrodes: Effect of particle size and volume fraction, International Journal of Hydrogen Energy, vol. 47, no. 73, pp. 31446-31458, doi: 10.1016/j.ijhydene.2022.07.071.
[29] Y. Xiang, Y. Da, N. Shikazono, Z. Jiao, 2020. Quantitative study on solid oxide fuel cell anode microstructure stability based on 3D microstructure reconstructions, Journal of Power Sources, vol. 477, pp. 228653, doi: 10.1016/j.jpowsour.2020.228653.
[30] Z. Jiao, E. P. Busso, N. Shikazono, 2020. Influence of polarization on the morphological changes of nickel in fuel electrodes of solid oxide cells, Journal of the Electrochemical Society, vol. 167, no. 2, pp. 024516, doi: 10.1149/1945-7111/ab6f5b.
[31] M. Kishimoto, H. Onaka, H. Iwai, M. Saito, H. Yoshida, 2019. Physicochemical impedance modeling of solid oxide fuel cell anode as an alternative tool for equivalent circuit fitting, Journal of Power Sources, vol. 431, pp. 153-161, doi: 10.1016/j.jpowsour.2019.05.057.
[32] S. Lan, R. Lin, M. Dong, K. Lu, M. Lou, 2023. Image recognition of cracks and the effect in the microporous layer of proton exchange membrane fuel cells on performance, Energy, vol. 266, pp. 126340, doi: 10.1016/j.energy.2022.126340.
[33] M. Tan, B. Bolas, E. Lawrence, P. Crozier, 2020. Tracking Atomic Scale Oxygen Exchange in Dynamic Structure of CeO_2 Nanoparticle Surfaces, Microscopy and Microanalysis, vol. 26, no. S2, pp. 1760-1761, doi: 10.1017/S1431927620019248.
[34] X. Yan, J. Yang, T. Salami, 2025. Classification of Indian classical dances using MnasNet architecture with advanced polar fox optimization for hyperparameter optimization, Scientific Reports, vol. 15, no. 1, pp. 18624, doi: 10.1038/s41598-025-03054-z.
[35] J. G. Rix, B. Mo, AY. Nikiforov, U. B. Pal, S. Gopalan, S. N. Basu, 2021. Quantifying percolated triple phase boundary density and its effects on anodic polarization in Ni-infiltrated Ni/YSZ SOFC anodes, Journal of The Electrochemical Society, vol. 168, no. 11, pp. 114507, doi: 10.1149/1945-7111/ac3599.
[36] F. Serbet, T. Kaya, 2025. New comparative approach to multi-level thresholding: Chaotically initialized adaptive meta-heuristic optimization methods, Neural Computing and Applications, vol. 37, no. 14, pp. 8371-8396, doi: 10.1007/s00521-025-11016-9.
[37] C. Chen, Y. Gao, 2024. Using multi-threshold non-local means joint distribution method to analysis the spatial distribution patterns of binder and fibers in gas diffusion layers of fuel cells, Applied Energy, vol. 358, pp. 122513, doi: 10.1016/j.apenergy.2023.122513.
[38] A. Sciazko, T. Shimura, Y. Komatsu, N. shikazono, 2021. Ni-GDC and Ni-YSZ electrodes operated in solid oxide electrolysis and fuel cell modes, Journal of Thermal Science and Technology, vol. 16, no. 1, pp. JTST0013-JTST0013, doi: 10.1299/jtst.2021jtst0013.
[39] K. Yamazaki, M. Kishimoto, H. Iwai, 2024. Gas-species dependence of permeation flow in solid oxide fuel cell porous anodes fabricated with pore formers, Journal of Thermal Science and Technology, vol. 19, no. 1, pp. 23-00492, doi: 10.1299/jtst.23-00492.
[40] M. l. Mendelson, 1969. Average grain size in polycrystalline ceramics, Journal of the American Ceramic society, vol. 52, no. 8, pp. 443-446, doi: 10.1111/j.1151-2916.1969.tb11975.x.
[41] Z. Zhang, X. Zhang, H. Du, K. Xu, X. Ma, S. Shuai. 2025. Decoupled Analysis of Microstructure Parameters for Sofc Anode Functional Layer Based on 3d Reconstruction and Lattice Boltzmann Method, doi: 10.2139/ssrn.5271924.

[42] M. Kishimoto, 2013. Three-dimensional microstructure of solid oxide fuel cell anode: observation, quantification, and application to numerical analysis, [Doctoral dissertation, Kyoto University]. Kyoto University Research Information Repository, https://doi.org/10.14989/doctor.k17561.
[43] T. Hamann, L. Zhang, Y. Gong, G. Godbey, J. Gritton, D. McOwen, G. Hitz, E. Wachsman, 2020. The Effects of Constriction Factor and Geometric Tortuosity on Li-Ion Transport in Porous Solid-State Li-Ion Electrolytes, Advanced Functional Materials, vol. 30, no. 14, pp. 1910362, doi: 10.1002/adfm.201910362.
[44] S. S. Rathore, 2017. Investigation of Microstructural and Carbon Deposition Effects in SOFC Anodes Through Modelling and Experiments, [Doctoral dissertation, Curtin University]. https://core.ac.uk/download/pdf/195692743.pdf.
[45] P. Vijay, 2021. Software application for image based solid oxide fuel cell electrode microstructure characterisation, [Online]. Available: https://github.com/Devetree/SOFC-IMG.
[46] Y. X. Zhang, J. Ma, M. Yan, 2016. Is 2D stereological method good enough for quantification of solid oxide fuel cell electrode microstructure? Science Bulletin, vol. 61, pp. 1313-1316, doi: 10.1007/s11434-016-1079-x.
[47] K. S. Rao, V. Tirth, H. Almujibah, A. H. Alshahri, V. Hariprasad, N. Senthilkumar, 2023. Optimization of water reuse and modelling by saline composition with nanoparticles based on machine learning architectures, Water Science & Technology, vol. 87, no. 11, pp. 2793-2805, doi: 10.2166/wst.2023.161.
[48] L. Yuan, J. Sun, L. Quan, HY. Shum, 2008. Progressive inter-scale and intra-scale non-blind image deconvolution, Acm Transactions on Graphics (TOG), vol. 27, no. 3, pp. 1-10, doi: 10.1145/1360612.1360673.
[49] I. Kandel, M. Castelli, L. Manzoni, 2022. Brightness as an augmentation technique for image classification, Emerging Science Journal, vol. 6, no. 4, pp. 881-892, doi: 10.28991/ESJ-2022-06-04-015.
[50] D. Banik, S. Pal, M. N. B. Naskar, A. Bandyopadhyay, 2022. Transformer Based Technique for High Resolution Image Restoration, 2022 OITS International Conference on Information Technology (OCIT), pp. 558-563, doi: 10.1109/OCIT56763.2022.00109.
[51] M. Dehghananari, M. Hosseinjanizadeh, 2024. Investigation of the Support Vector Machine (SVM) algorithm for land use changes, a case study of Kerman Province, Iran, Journal of Geological Remote Sensing, vol. 2, no. 1, pp. 1-14, doi: 10.48306/jgrs.2024.467600.1009.
[52] T. Shimura, Z. Jiao, N. Shikazono, 2016. Dependence of solid oxide fuel cell electrode microstructure parameters on focused ion beam – Scanning electron microscopy resolution, International Journal of Hydrogen Energy, vol. 41, no. 47, pp. 22373-22380, doi: 10.1016/j.ijhydene.2016.09.006.
[53] A. Faes, A. Hessler-Wyser, D. Presvytes, CG. Vayenas, J. Van Herle, 2009. Nickel-zirconia anode degradation and triple phase boundary quantification from microstructural analysis, Fuel cells, vol. 9, no. 6, pp. 841-851, doi: 10.1002/fuce.200800147.
[54] S. Jang, Y. Kang, K. T. Bae, S. H. Park, Y. J. Park, D. Kim, H. Yu, H. Kim, S. Yu, K. T. Lee, 2025. Digital Twin of Solid Oxide Electrochemical Cells: From 3D Microstructure Reconstruction to Multiphysics Modeling, Advanced Energy Materials, pp. e03842, doi: 10.1002/aenm.202503842. [55] C. J. C. Otic, I. Kinefuchi, 2025. Machine learning-driven 3D reconstruction of PEMFC catalyst layers from FIB-SEM imaging, Journal of Power Sources, vol. 651, pp. 237556, doi: 10.1016/j.jpowsour.2025.237556.